Acta Geotechnica (2011) 6:105–117
DOI 10.1007/s11440-011-0139-2

RESEARCH PAPER

Centrifuge model test on the face stability of shallow tunnel

Gregor Idinger · Pelin Aklik · Wei Wu · Ronaldo I. Borja

Received: 11 October 2010 / Accepted: 18 May 2011 / Published online: 22 June 2011

Abstract This paper is an investigation of face stability on a small-scale tunnel model in a geotechnical centrifuge. By making use of symmetry, half of the tunnel cross section was considered. The support at excavation face was provided by a piston, which was adjusted during flight. Some aspects on the collapse at tunnel face are investigated for different overburden pressures: failure mechanism, surface settlement, stress acting at tunnel face, and the required face support counteracting the earth pressure. Ground deformation was observed through a transparent wall and measured by digital image correlation. The results from centrifuge model tests were compared with theoretical models.

Keywords Centrifuge modeling · Digital image correlation · Face stability · Shallow tunnel

1 Introduction

As urban expansion increases and available land decreases, new transportation and service networks need to be placed underground. For easier access, in many cases, tunnels are constructed at shallow depth and in the immediate vicinity of existing infrastructure (e.g., foundations). Hence, tunnels in urban regions are often constructed in soft ground conditions. The inherent problem associated with underground construction in soft ground is that underground excavation alters the stress field in the surrounding material. Soil strata cannot bear superimposed loads, and thus, ground deformation occurs. Most susceptible to collapse is the tunnel face, which can result in a chimney-shaped failure [9]. Usually, failure initiates near tunnel face and propagates toward ground surface until either a stabilizing arch is formed, or it reaches ground surface causing cave-in. The latter is severe for shallow constructions. In urban regions, even small surface settlement can cause damage to surface buildings.

Shallow tunnels in soft ground are usually driven by shield tunnel boring machine (TBM). Different techniques for face support have been developed, including EPB (Earth Pressure Balance) shield and slurry shield. They have something in common in that support is applied by a pressurized medium.

Figure 1 illustrates the typical stress condition at tunnel face. The support pressure counteracts the effective earth pressure and water pressure. While water pressure can be predicted reliably, theoretical models provide a wide range of earth pressures. Tunnel construction with a support pressure according to a linear increase in earth pressure with depth is time- and cost-intensive. Moreover, a high pressure may induce blowout and heave of the ground. Experience has shown that tunnel construction with a face support pressure lower than the pressure given by the linear stress distribution can be successfully employed in soft ground at shallow depth without excessive ground deformation [20]. However, the extent of ground movement associated with a reduced support pressure is not yet well known.

The face stability at shallow depth is a popular topic of research of the last decades and until today [3, 8, 16, 19,

Paper presented at the International Workshop on Multiscale & Multiphysics Processes in Geomechanics, June 23–25, 2010, Stanford University.

G. Idinger (✉) · P. Aklik · W. Wu
Institute of Geotechnical Engineering, Universität für Bodenkultur, 1180 Vienna, Austria
e-mail: gregor.idinger@boku.ac.at

R. I. Borja
Department of Civil and Environmental Engineering, Stanford University, Stanford, CA 94305, USA

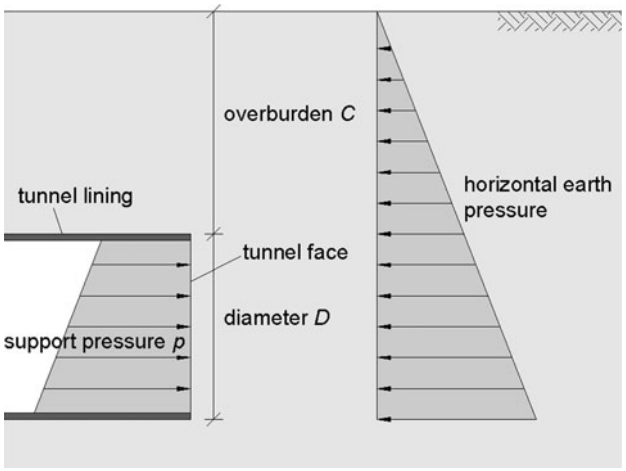

Fig. 1 Sketch of simplified stress condition at excavation face: face support pressure, p, balancing the horizontal earth pressure ensuring stability at excavation face (linear increase in earth pressure assumed)

21, 23, 26, 27, 35]. Among others, Leca and Dormieux [15] proposed a failure criterion for the tunnel face in cohesive and frictional soil. Chambon and Corte [5, 6] reported on centrifuge model tests where the support pressure for face stability was measured. Despite the wide choice of proposed models, only a few of them have been applied in tunnel projects (e.g., Horn [9], Leca and Dormieux [15], Anagnostou and Kovári [1, 2]). Only limited evidence for their quality exists. Driving a shallow tunnel is still mainly based on experience, since experimental data are rare and well-documented projects involving collapse are barely available.

To further assess the capability of theoretical models, centrifuge tests were performed on a small-scale model in dry sand. The influence of the overburden was examined for three overburden-to-diameter ratios C/D, at 1.5, 1.0, and 0.5. Collapse at tunnel face was induced in a displacement-controlled manner by pulling a plate, which provided the support, back into the tunnel. The prefailure behavior and ground movement during failure were recorded and analyzed by digital image correlation. The extent of failure mechanism and surface settlement was investigated, and the pressure at failure was measured. Finally, an attempt to identify the depth at which a silo effect emerges was made.

2 Centrifuge model

2.1 Centrifuge technique and scaling laws

The centrifuge technique was established in the early 1930s by Philip B. Bucky [4, 17], who tested the geomechanical behavior of a small-scale model under increased stress,

Table 1 Selected scaling factors for centrifuge modeling

Quantity	Dimension in prototype	Dimension in centrifuge model at n times g
Gravity	1	n
Stress/strain	1	1
Length	1	$1/n$
Force	1	$1/n^2$
Density	1	1
Unit weight	1	n
Acceleration	1	n
Time (consolidation)	1	$1/n^2$

examining failure mechanism relating to the ultimate limit state. In recent years, with new detailed and continuous deformation measurement systems, the centrifuge technique has been adopted increasingly for studying prefailure deformation. Physical model tests in the centrifugal field allow for well-controlled laboratory conditions, which is relevant for conducting parametric studies and investigating failure mechanisms. Observations from the small-scale model are related to the prototype using well-established scaling laws (Table 1). Centrifuge model tests have been shown to be valuable in revealing mechanisms of soil deformation and collapse, as well as for validating numerical models [29].

The mechanics of tunnel face instability is a gravity-dependent phenomenon. Strength and stiffness of a soil vary with the applied stress (i.e., influence of depth). While large-scale models represent true soil response, they are expensive to perform. On the other hand, a small-scale model at 1 g is less expensive, well controllable, highly instrumented, and easier to perform in series. Yet, these experiments do not fully represent correct prototype behavior, since the stress level is much lower than in the field. In order to simulate a correct prototype situation in the laboratory, it is crucial to replicate the in situ soil stress field properly.

In a centrifuge, the small-scale model is subjected to an acceleration field n times greater than earth's gravity acceleration constant, g. Thus, each soil particle in the model weights n times more. As a result, the gradient of body stress within the small-scale model will now be similar to the prototype n times larger, ensuring similarity of effective stress at equivalent depth in model and prototype. This implies that a $1/n$ scale model will behave like its full-scale prototype if subjected to a centrifugal acceleration of n times g. Thus, gravity-dependant processes are correctly reproduced. Stress and strain in the prototype soil mass are preserved, and the strain–stress curve of the model is identical to one of the prototype.

Scaling laws are essential in order to transfer measured data from the small-scale model to the prototype. In the

prototype, vertical stress, σ_{vp}, acting in a material of density, ρ, at depth h_p is given by

$$\sigma_{vp} = \rho g h_p, \tag{1a}$$

while the vertical stress in the model, σ_{vm}, at depth h_m in the same material within the gravity field of n times g in the centrifuge is given by

$$\sigma_{vm} = \rho n g h_m \tag{1b}$$

As explained earlier, the basic scaling law is derived from stress similarity between the model and prototype. Thus, for $\sigma_{vm} = \sigma_{vp}$, the depth h_m is scaled by $h_m = h_p/n$. The obtained scaling factor for length (i.e., distance, displacement) is $1/n$. Table 1 presents a selection of scaling factors.

2.2 Issues of centrifuge technique

In a modeling process on reduced scale, it is generally rarely possible to replicate all details from the prototype. Thus, some approximations have to be made (e.g., simplified geometry). It is important to recognize that model studies are not perfect and to be aware of its limitation. Additional model imprecision can result from the centrifuge technique. Shortcomings, often referred as scaling effects, are evaluated in this section.

First of all, in civil engineering, the earth's gravity, g, is simplified as being constant.[1] However, the acceleration field generated in a centrifuge slightly differs from the prototype gravitational field because the acceleration force, a, is proportional to the radius

$$a = ng = \omega^2 r \tag{2}$$

where ω is the angular velocity and r is the radius to the soil model. The distributions of vertical stress are compared in Fig. 2. The discrepancy turns out to be minor if the scale factor, n, is determined for the radius of the zone of interest (i.e., axis of tunnel). According to Taylor [29], if the ratio of model height, h_m, and effective centrifuge radius, R_e, (where $R_e = R_t + h_m/3$; with R_t as radius to top of the model) is less than 0.2, the maximum error in the stress profile is less than 3%. For our tests, the ratio is between 0.14 and 0.21, which makes the error negligible.

Secondly, as the acceleration field is oriented toward the center of rotation. The direction of acceleration changes relative to a vertical plane (i.e., horizontal section of the model during flight) across its width (Fig. 3). Thus, a small lateral acceleration component affects the model soil. The model should be designed in a way to enable major events

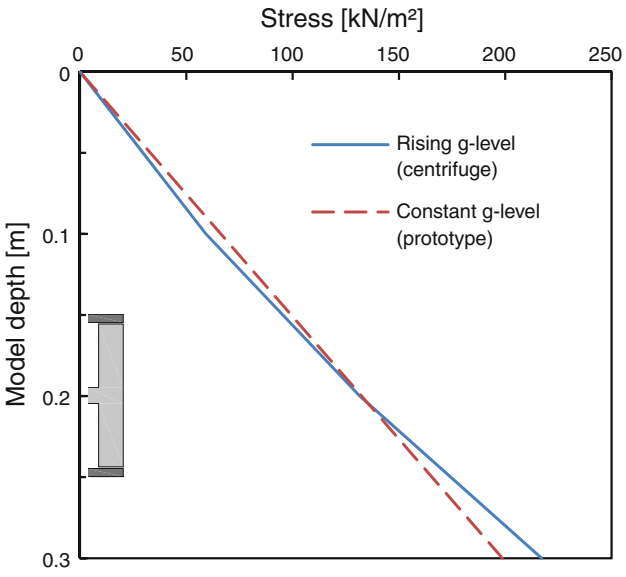

Fig. 2 Comparison of stress variation over depth in a centrifuge model and its corresponding prototype ($C/D = 1.5$)

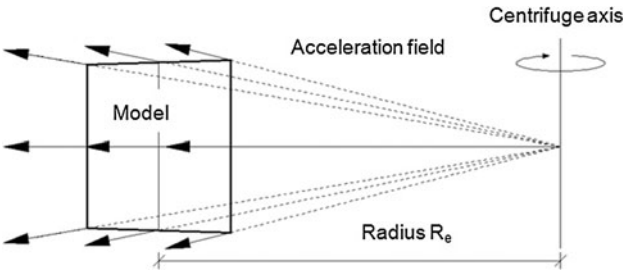

Fig. 3 Nonparallel orientation of acceleration forces dependent on the location in the centrifuge model

occurring close to the center of the plane, where the vertical acceleration force is minimal.

Thirdly, an incorrect centrifuge gravity field appears when the resulting force of centrifugal force and earth gravity (which naturally appears also within the centrifuge) is not perpendicular to the model surface. This is caused by the frictional resistance in the pivots of the swinging basket. Therefore, the real upswing angle will always be smaller than the theoretical upswing angle. However, with an eccentric adjusted model mass, the effect can be minimized (cf. Sect. 2.4).

An important issue in small-scale modeling is how it can be justified if the size of soil particles is not reduced by the factor of n, as determined by the scaling factor for length. If doing so, in a 1/100 scale model, fine sand would represent medium gravel, and clay would represent fine sand. Of course, this cannot be correct since clay has different stress–strain characteristics than sand. Local effects of the soil grains would influence the model behavior rather than

[1] The variation in earth's gravity, g, according to Newton's law of universal gravitation, resulting from $g \sim r^2$, is negligible for the covered range of radius to earth's center of mass (i.e. depth).

the soil appearing as a continuum, like in the prototype. Thus, the prototype material is used for small-scale modeling.

To minimize scaling effects on soil-structure interaction due to the grain size, some critical ratios of characteristic dimension of the structure to mean grain diameter, d_{50}, are available in the literature. The technical committee TC2 (Physical Modelling in Geotechnics) of the ISSMGE provides a catalog of collected scaling laws and similitude questions in centrifuge modeling [30]. For the soil-structure interaction at tunnel face, the relation $D/d_{50} > 175$ is recommended [7]. With the model sand used in the centrifuge tests, a D/d_{50} ratio of about 125 was reached. Therefore, some caution is needed to appreciate the test results. Furthermore, grain size effects have been detected on the development of shear band patterns in a trap door test simulating chimney collapse [22, 24, 34]. While collapse load is not sensitive to the grain size, the propagation of a collapsing chimney is sensitive to B/d_{50}, even for a ratio as large as 1,000, which cannot be modeled at small scale [13, 28, 39]. For these reasons, a small-scale model behaves stiffer than its prototype.

A proper method for checking scale effects is "modeling of models". This is particularly useful when no prototype is available to verify the centrifuge model test results. Centrifuge models of different scales are tested at the appropriate acceleration level (e.g., scale of 1/50 at 50 g and scale of 1/100 at 100 g). Thus, they correspond to the same prototype. These models should predict the same behavior and provide a check on the modeling process. However, this technique was not implemented in this paper, due to geometric limitations.

2.3 Measurement of soil deformation with digital image correlation

Digital Image Correlation, DIC (also referred to as Particle Image Velocimetry, PIV) was adopted to quantify soil movement in the prefailure and regime. This technique enables displacement measurement at potentially thousands of points of the model with high accuracy [36–38].

DIC operates by tracking the soil texture (particular and random orientation of grains in the model) within a digital image and through successive images. For this purpose, the initial image is subdivided into a mesh of patches. Each patch covers a few sand grains and is characterized by a unique spatial distribution of gray-scale values. Consider one patch located at coordinates (u_i, v_i) in image i. To find the location of this patch in the subsequent image i + 1, the correlation between the patch from image i (time = t_i) and its new position within a search zone around the original patch position in the subsequent image i + 1 (time = t_{i+1}) is evaluated (Fig. 4). At each position, the correlation is calculated, resulting in a map of "degree of match" over the entire search zone. The location with the highest correlation indicates the new position of the patch (u_2, v_2). For a satisfying adjustment, the correlation peak has to exceed the random noise distortion. Otherwise, so-called wild vectors are produced. The exact location of the correlation peak is established to subpixel precision by interpolation around the peak value [36].

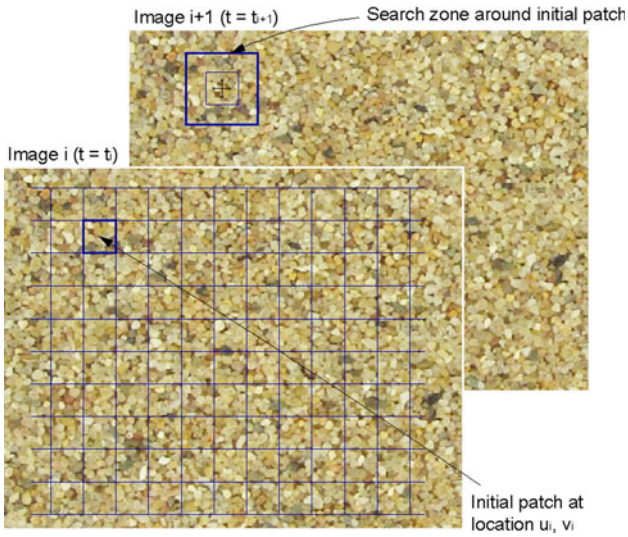

Fig. 4 Principle of digital image correlation

The use of DIC is feasible if the soil possesses suitable texture, otherwise texture has to be added by tracer particles. Natural sand fulfills this requirement (variable shaded grains, light and shadows form between adjacent grains when sand becomes illuminated) [37]. Thus, commonly applied distractive target markers or colored soil layers within the observed soil domain are not required.

A series of digital images, taken by a digital still camera, is the underlying data for the DIC calculation. The soil deformation between two images is calculated in image space. Displacement vectors are translated from image space (units of pixel) to real space (e.g., units of millimeter) by camera calibration. The calibration includes corrections for effects of lens distortion, camera orientation, and refraction through the observation window. Therefore, stationary reference points with defined real space coordinates are drawn onto the acrylic. For a satisfying correction of image distortion, reference points have to be distributed over the whole field of view. At least 15 reference points are recommended [33]. However, one should be aware that the area covered by a reference point is not visible and therefore interpreted as being stationary. This constraint should not affect zones of great interest, like a slip surface. Thus, knowledge of the anticipated failure mechanism is auxiliary, e.g., gain from a pretest or basic soil mechanic calculation.

The precision of digital image correlation depends strongly on patch size and less on the image content [36]. A larger patch size would lead to improved precision, though the number of measurement points within an image is smaller. Thus, larger patches "smear" the measured data in the area of a high shear strain gradient (i.e., slip surfaces are not detected). For successful deformation measurement, the smallest strain throughout the field of interest must be captured. Assuming a prefailure deformation of 0.01% is within a zone of a few centimeters, the required resolution in detecting movement is a few micrometers. In literature, uncertainties of 100 μm are thought to be sufficient to compare the experimental observations with results of numerical analyses [10, 18]. In a screening test, where a photograph of sand grains was subjected to pure horizontal displacement, a standard error of 16 μm (0.08%) was evaluated. Thus, the achieved accuracy of the system was found to be satisfactory.

2.4 Centrifuge and material properties

Tests were carried out with the geotechnical centrifuge in Vienna. The beam centrifuge has a nominal radius of 1.3 m and is capable of generating a maximum acceleration of up to 200 g at a load capacity of 10,000 g-kg. The platform size is 0.54×0.56 m^2. The model tunnel was placed inside a box made of aluminum plates of thickness 15 mm with inner dimensions of 440 × 155 × 400 mm (width × depth × height). An acrylic plate with a thickness of 30 mm was attached as front wall.

The eccentric test assembly was mounted with the heavy part (soil-filled model box) on the inner side of the swinging platform adjacent to the centrifuge axis (lower side during flight). Therefore, a higher upswing angle of the swinging platform was achieved, minimizing the effect of pivot friction of the swinging platform. An upswing angle of about 88° was observed (frictionless upswing angle at 50 g is arctan (50/1) = 88.9°).

The model sand was mixed by two grain fractions with a mean grain diameter of about 0.8 mm ($C_u = 3.70$) (Fig. 5). A loose state was achieved by pluviating sand from a height of about 300 mm, resulting in an initial dry density, ρ_d, of about 1.5 g/cm^3 (initial void ratio $e = 0.77$, $e_{min} = 0.61$, $e_{max} = 0.84$). A friction angle of 34 degrees was obtained from direct shear test.

2.5 Modeling of a shallow tunnel

The tunnel model had a circular cross section. By making use of symmetry, only half of the tunnel cross section was considered. The tunnel was placed adjacent to the acrylic wall, which is the tunnels vertical plane of symmetry. The tunnel lining was modeled by a half aluminum cylinder

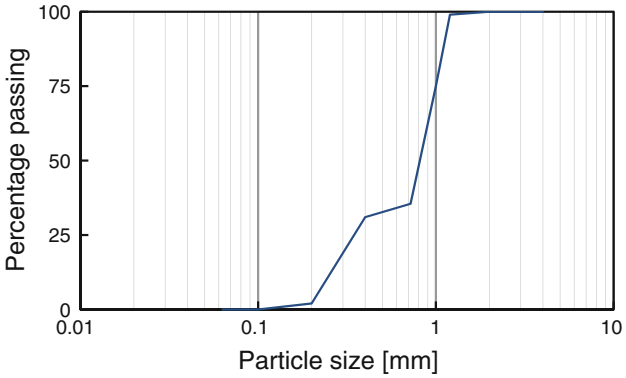

Fig. 5 Grain-size distribution curve for experimental soil

with an outer diameter of 100 mm and wall thickness of 3 mm. The position of the tunnel with reference to the boundaries of the model box is shown in Fig. 7a, b. The distance to the back wall was about 1 D, to the right wall about 3 D, to the left wall about 1.5 D, and to the bottom plate about 0.5 D. Thereby, the influence of boundary conditions on the soil behavior was minimized.

Face support was provided by a semi-circular face plate, which could be moved back or forth by means of a linear actuator, operating as a piston. To trigger collapse, this piston was moved backward. A load cell and an LVDT transducer were attached behind the face plate to measure the support pressure and piston displacement (Fig. 7c).

The face plate was slightly smaller than the lining to reduce the friction between the lining and the plate. Moreover, Teflon strips were adhered to the inner side of the lining and the perimeter of the face plate to reduce friction. However, the friction could not be completely eliminated under elevated acceleration. As a consequence, the friction was estimated through a calibration test without soil, where the friction force was measured by moving the piston backward under the same elevated acceleration level as the collapse tests were conducted. Figure 6 shows the calibration test, where the negative sign stands for tensile force. A constant friction force of about 8 N was used to correct the measured data from the load cell.

To prevent ingress of sand (additional source of friction), the perimeter of the tunnel face was covered with cling foil. The cling foil was fitted with enough slackness to avoid an influence on the soil-tunnel face interaction during the backward displacement of the face plate.

2.6 Instrumentation

Due to small inner dimensions of the tunnel model, only miniature measuring devices could be used. The active earth pressure on the face plate was measured by a load

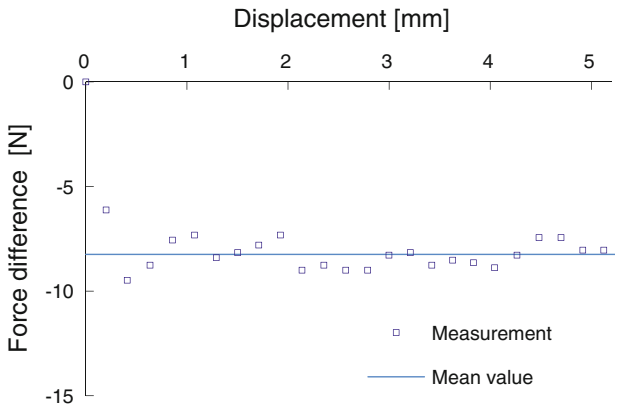

Fig. 6 Calibration of face plate and tunnel shell at 50 g

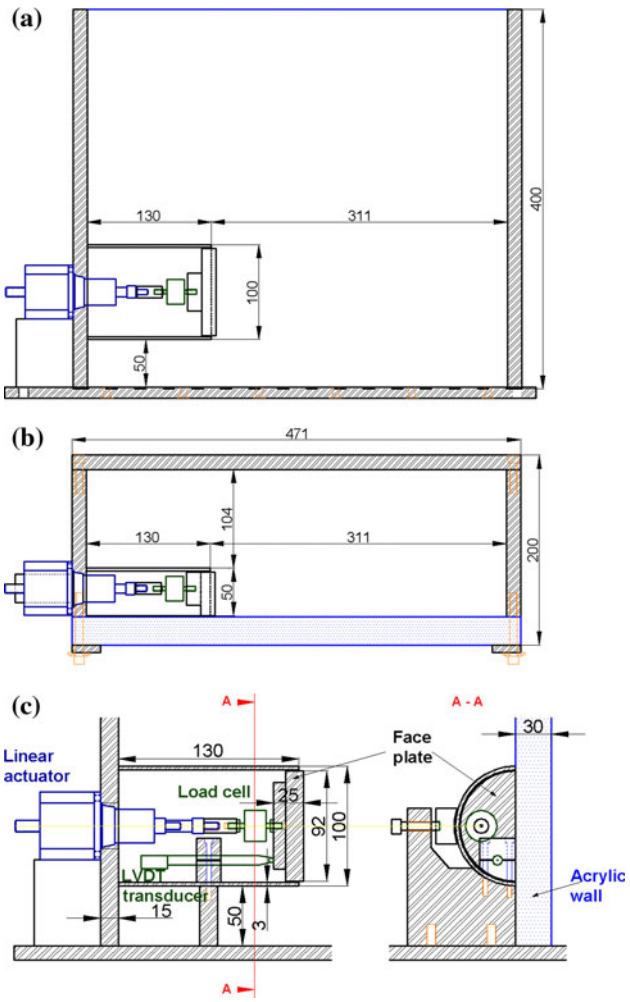

Fig. 7 Schematic sketch of tunnel model: **a** front view and **b** top view on model box, **c** longitudinal section and cross section A-A of the tunnel

cell. The mean pressure was calculated by dividing the measured force by the area of the tunnel face. Compression and tensile forces were measured to an accuracy of 0.12 N. The LVDT transducer measured the axial displacement of the tunnel plate with an accuracy of 0.625 µm.

A linear actuator converted the rotation of a step motor into translational displacement. Thereby, the face support was manipulated during flight by remote control. One step (rotation of 1.8°) was equal to a movement of 10.5 µm. The tunnel plate was moved back at a constant rate of one step per 5 s.

A digital still camera (CCD) was attached to a rigid frame, with the camera lens inserted through a tightly fitting aluminum block. In addition, the small gap between lens and fitting was filled with layers of Teflon strips to provide a stable mount. This arrangement avoided the downward displacement of the lens due to the increased gravity level, and preserved a constant image frame during flight (Fig. 8). The distance from camera lens to the plane of observed soil deformation behind the acrylic wall was approximately 260 mm, providing a field of view of about 350 × 250 mm. Pictures were taken at a resolution of 3456 × 2592 pixels, coming up to a size of 9 MP. At this resolution, 1 mm had an extent of about 10 pixels. By that, a sand grain with a diameter of 1 mm was expressed by about 80 pixels. With the chosen patch size for image correlation of 32 × 32 pixels, one patch includes about 10 sand grains. This patch size assured high accuracy as well as high spatial resolution.

To receive a photo series over the whole experiment, it was essential to have a remote control software for the camera and thereby a connection to a computer within the centrifuge. Therefore, a netbook was mounted close to the centrifuge axis since the acceleration force decreases at smaller radii (i.e., < 10 g during a 50 g test). The netbook was operated by a computer in the control room via Ethernet connection over slip rings.

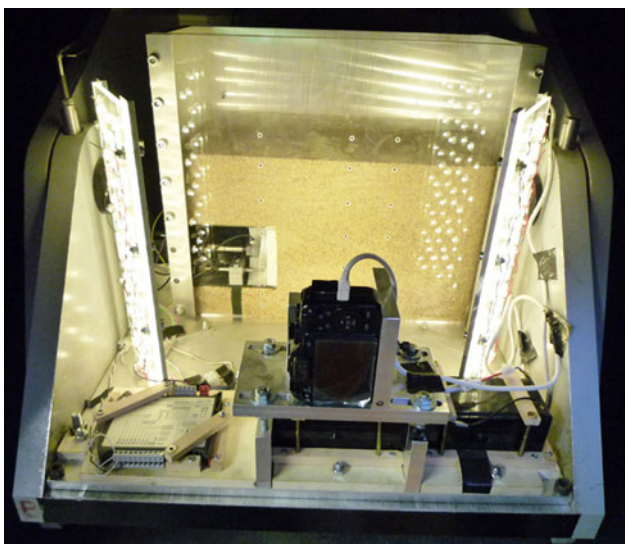

Fig. 8 Model assembly mounted on swinging platform

3 Results

The experimental results on required face support pressure, failure initialisation mode, failure propagation, ground deformation, and surface settlement are presented in this section.

Centrifuge model tests have been carried out for three overburden-to-diameter ratios: $C/D = 1.5$ (test T1, T2), $C/D = 1.0$ (T3, T4, T5), and $C/D = 0.5$ (T6). Tests T2, T4, and T5 were performed for model validation. The model was accelerated up to 50 g in progressive steps, which corresponds to a prototype tunnel of 5.0 m in diameter. The prototype overburden above tunnel crown was about 7.5, 5.0, and 2.5 m, respectively. The tests were stopped at a piston displacement, d_p, of 5 mm (equal to 5% of D).

3.1 Support pressure

The curves in Fig. 9 illustrate the measurements from the load cell over piston displacement. Results are expressed for support pressure, p, and normalized pressure, N_0 $[p/(\gamma_d D)]$, at which measured pressure, p, was divided by the unit weight, γ_d, and tunnel diameter, D.

The initial stress state at 50 g can be read off from Fig. 9 for a zero displacement (14–28 kN/m^2). The initial stresses gave rise to an earth pressure coefficient of about 0.2, which is smaller than expected according to Jaky. This difference is ascribed to a small displacement of the piston during acceleration. Immediately after initialization of piston displacement, the pressure dropped remarkably, recording the active earth pressure at tunnel face. As the displacement continued, the pressure approached a more or less constant value on the order of 5–9 kN/m^2. This value was interpreted as the minimal pressure required for face stability. The unsteady development of the pressure at T6 was explained by local friction. Two tests (T3, T4) had to be stopped before reaching final piston displacement due to technical problems. Nevertheless, before aborting the test, the measured pressure was similar to the comparable test of T5.

3.2 Ground deformation

Results from DIC are presented in Fig. 10, 11, 12, and 13. Inspection of the displacement fields in Fig. 10 and 11 shows some gaps due to the removal of wild vectors which occurred specifically in regions with large shear strains.

The displacement field for different overburden-to-diameter ratios is compared in Fig. 10. For all overburden pressures, the failure mechanism can be clearly observed. At the elevation of tunnel crown, the failure was of similar width. For the smallest overburden of half the tunnel diameter, failure propagated vertically toward the surface. With increasing overburden, the failure zone widened up, and the failure mechanism was less defined.

Figure 11a illustrates the development of the displacement field for $C/D = 1.5$ at piston displacement increments of $\Delta d_p = 0.5$ mm. Figure 11b illustrates the development of the displacement field for $C/D = 0.5$. For the latter, ground movement appeared in a narrow vertical band only.

The failure mechanism can be clearly observed in the shear strain field (Fig. 12). The collapse mode was similar for all overburden pressures: two well-defined slip surfaces arose, one at the tunnel invert and one at the tunnel crown.

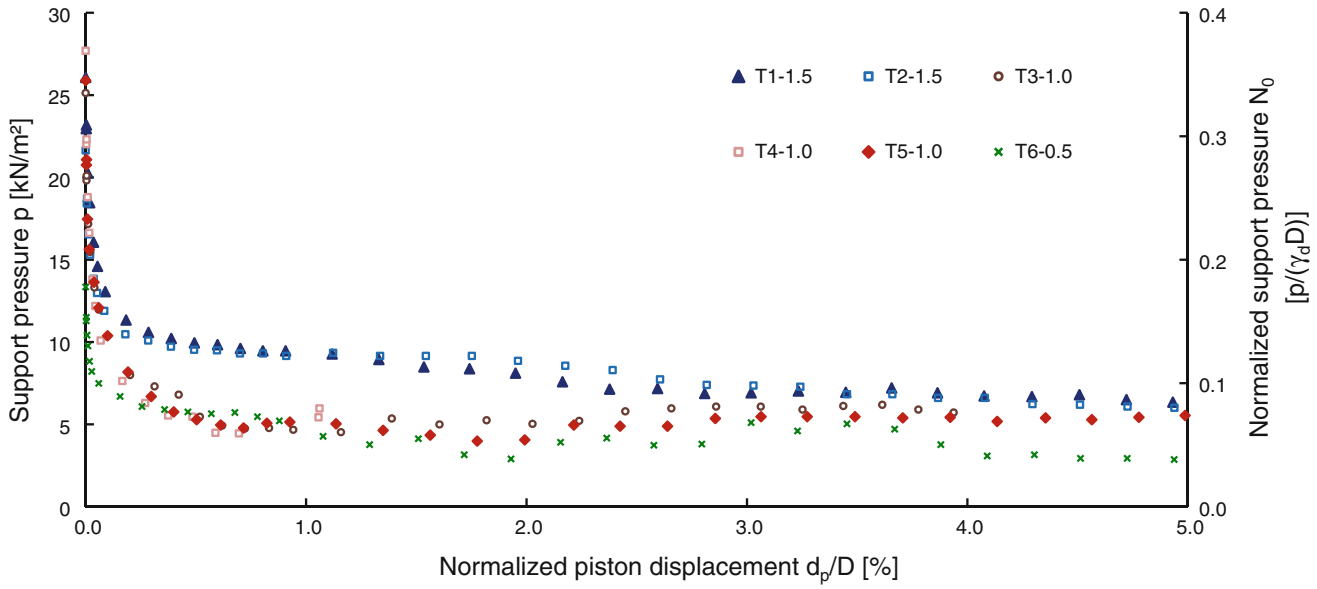

Fig. 9 Measured pressure at the face plate as a function of piston displacement

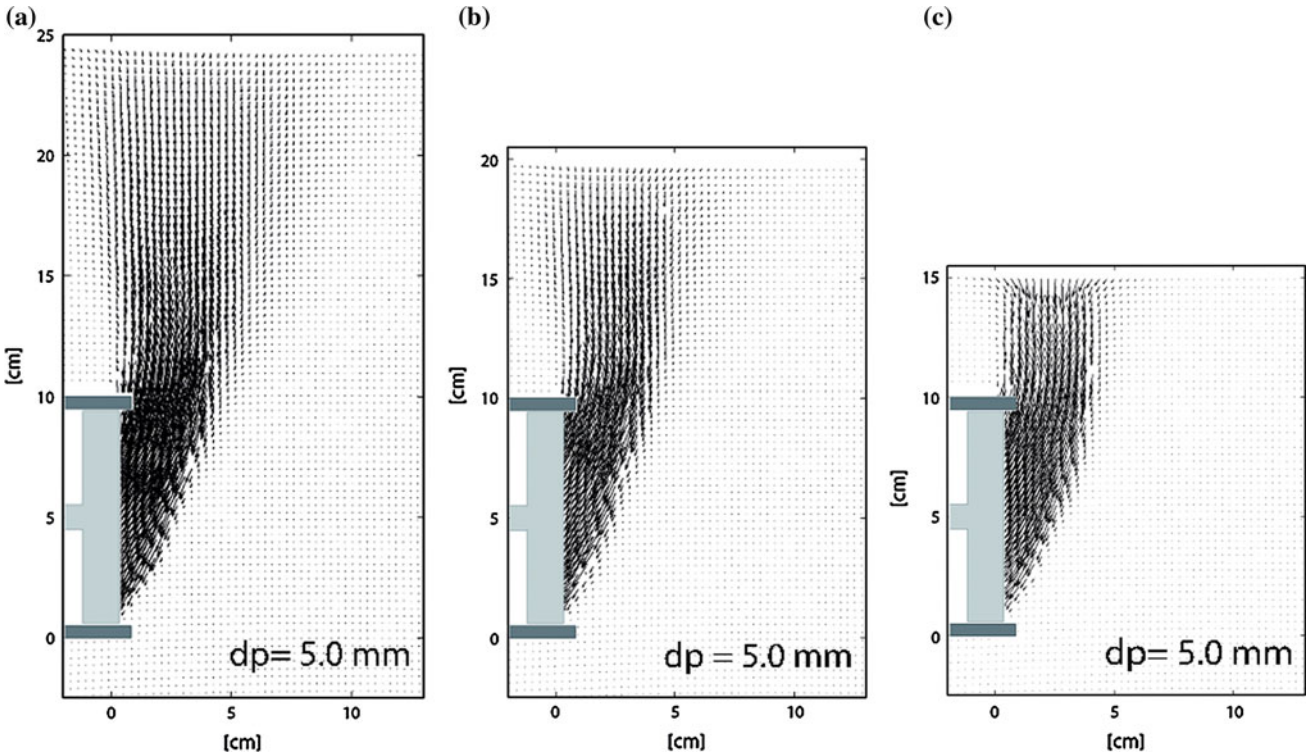

Fig. 10 Displacement field after piston displacement of 5 mm for different overburden-to-diameter ratios: **a** $C/D = 1.5$, **b** $C/D = 1.0$, and **c** $C/D = 0.5$; vector magnification of 2

The first slip surface started at the invert and propagated at an angle of 64–68° to the horizontal. As this slip surface reached the elevation of the tunnel crown, the second slip surface arose at the tunnel crown. Then, both propagated almost vertically to the ground surface.

The width of shear band spreads over approximately 10 mm or about 12 times d_{50}.

Surface settlement in the longitudinal cross section of the tunnel axis, derived from the DIC, is shown in Fig. 13. At $d_p = 5$ mm, a settlement of 1 mm at $C/D = 1.5$ and $C/D = 1.0$ and of about 5 mm at $C/D = 0.5$ was observed. Maximum settlement occurred at about 0.25 D ahead of the tunnel face. Only little settlement occurred behind the tunnel face. The extent of the settlement trough in the longitudinal direction was about half the tunnel diameter. The extent of the settlement perpendicular to the tunnel axis was about half the tunnel diameter for the examined symmetric half model.

A summary of the experimental findings and a comparison to other models are presented in Tables 2 and 3. Amongst others, the support pressure was compared with the kinematical approach proposed by Léca and Dermieux [15], where the first value corresponds to the upper bound and the second to the lower bound value of face collapse (Table 2). Some key information on the DIC is given in Table 3.

4 Interpretation and discussion

In some theoretical models, face support is assumed to be independent of the overburden pressure (e.g., [5, 11, 35]). This could not be verified by our centrifuge tests. For a piston displacement smaller than 3% of D, the effect of the overburden on the required support pressure can be clearly observed. The support pressure varied about 50% (6 kN/m^2 at $C/D = 0.5$ and $C/D = 1.0$, and 9 kN/m^2 at $C/D = 1.5$). For larger piston displacement (3–5% of D), the difference in support pressure became smaller, and the measured pressures converged at approximately 6 kN/m^2.

Because the active earth pressure on the tunnel face was relatively small, friction between the face plate and tunnel shell could have had a considerable effect. However, the range of required support pressure is in good agreement with other experimental investigations [5, 11, 25] and some proposed theoretical approaches [2, 15, 35] (Table 2). Some other models predict a pressure about twice as high [12, 14].

The observed soil deformation was similar to the failure mechanism, described by Horn [9], consisting of two block elements: a prismatic wedge in front of the tunnel face with a prismatic chimney on top reaching the ground surface, also verified in other experiments, e.g., Chambon and Corté [5]. A closer examination of Fig. 12 shows that the failure mechanisms differ from the theoretical model: the slip

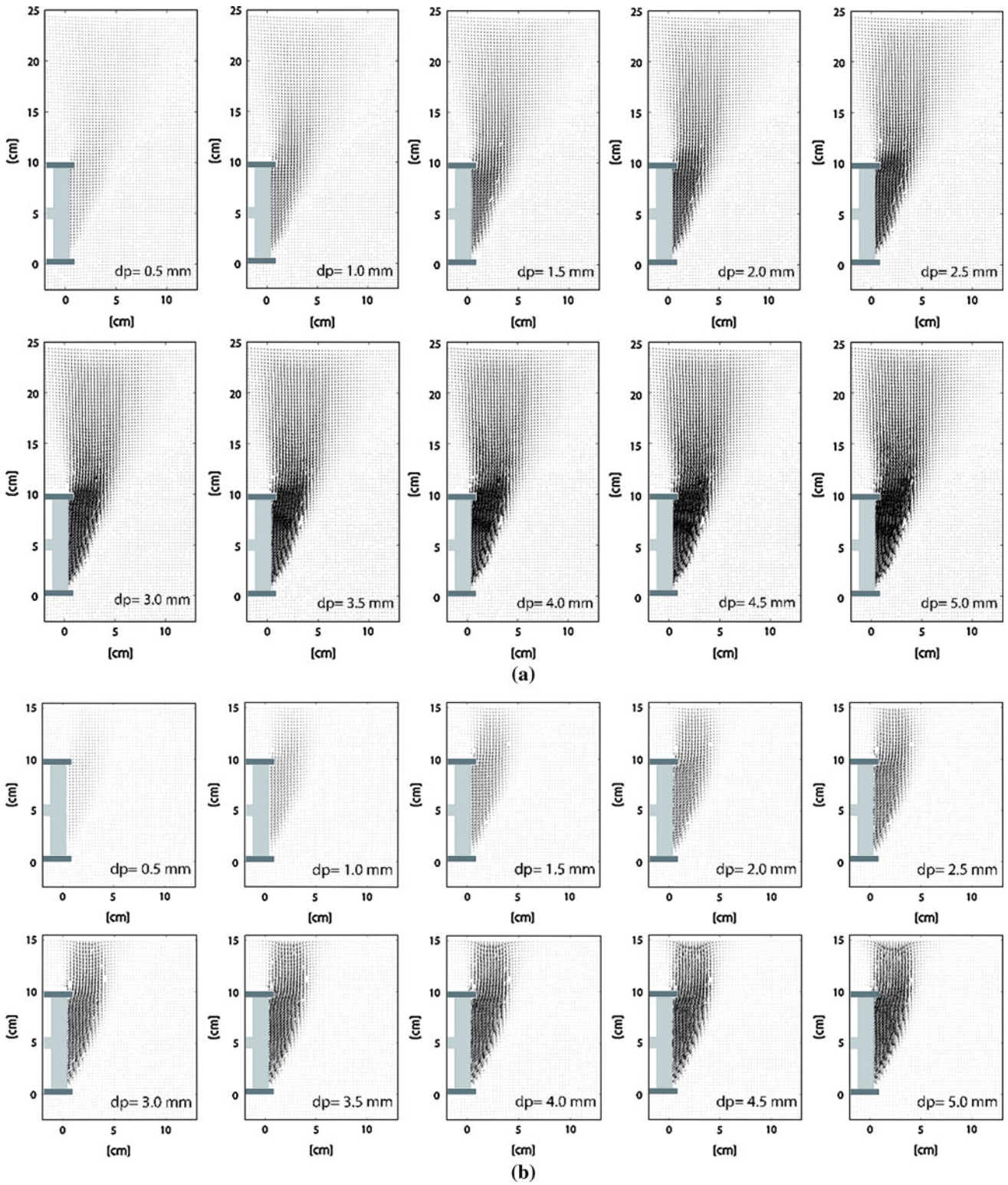

Fig. 11 Displacement field at **a** $C/D = 1.5$ and **b** $C/D = 0.5$ for piston displacement increments of $\Delta d_p = 0.5$ mm; vector magnification of 2

surface arising from the invert is curved instead of a straight line, and the movement of the wedge is orientated downward along its inclination instead of horizontal toward the tunnel. However, the different friction between soil and acrylic wall might have led to a reduced measurement of the soil displacement.

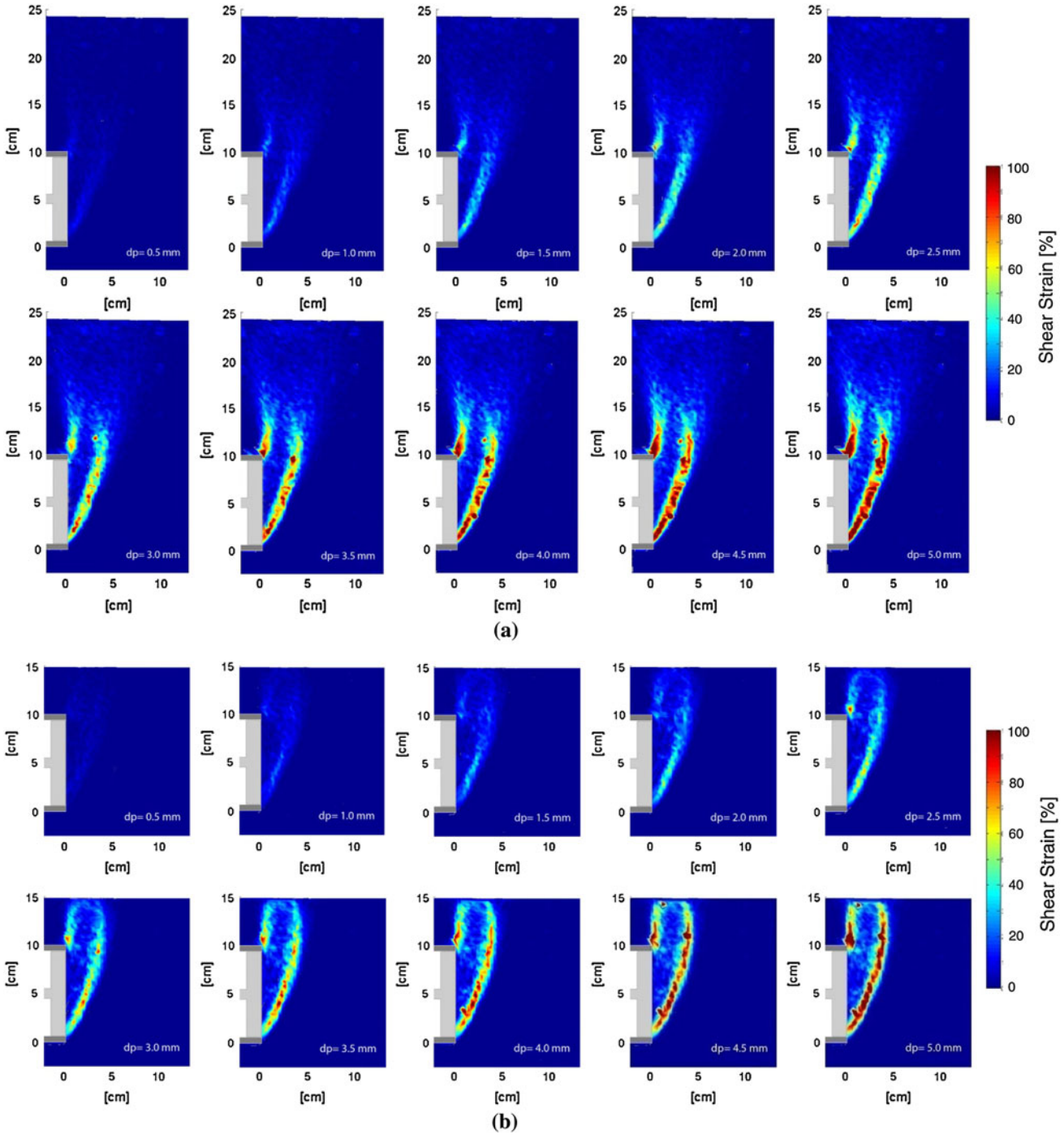

Fig. 12 Contours of shear strain at **a** $C/D = 1.5$ and **b** $C/D = 0.5$ for piston displacement increments of $\Delta d_p = 0.5$ mm

At higher overburden-to-diameter ratios, the extent of the chimney was wider, especially near the ground surface. This was partly due to the low initial density of sand in our tests. Centrifuge tests on dense sand in the literature show that the failure mechanisms are clearer delineated [11].

The failure mechanism, in particular the location of slip surfaces, could be observed after small piston displacement. In the field of shear strain, the propagation path of the two slip surfaces was already detected at a small piston displacement.

At the final face displacement of 5% of D only at the overburden ratio of $C/D = 0.5$, collapse propagated until ground surface. At the piston displacement of 3% of D, the rate of ground settlement increased to about 1.0 mm for $\Delta d_p = 0.5$ mm.

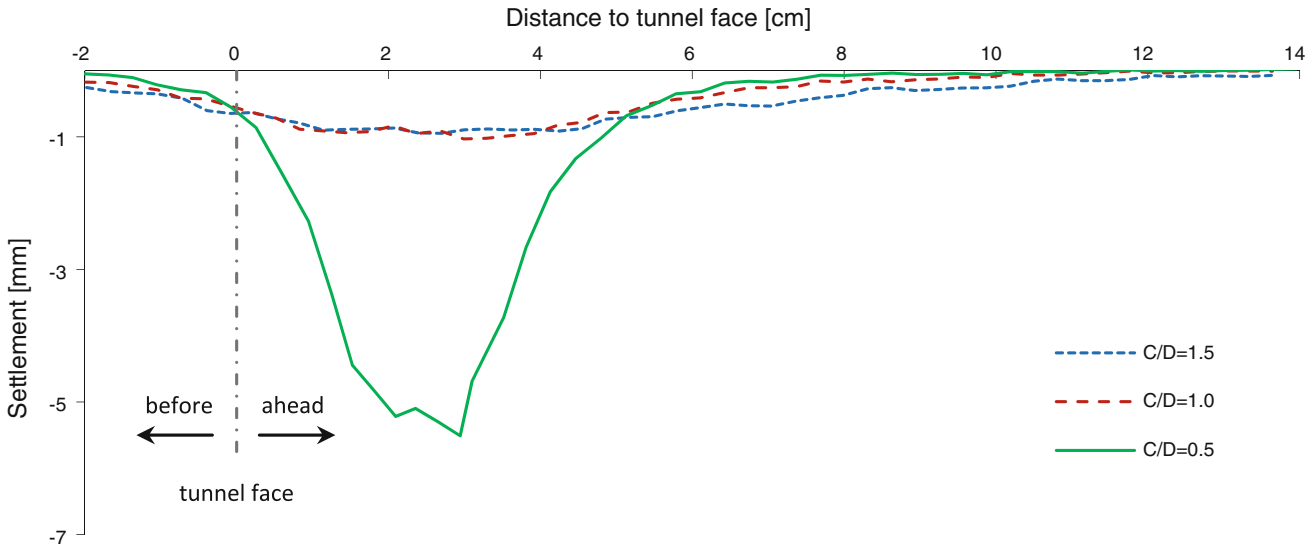

Fig. 13 Surface settlement at piston displacement $d_p = 5$ mm

Table 2 Summary on support pressure

Required support pressure [kN/m^2]	$C/D = 1.5$	$C/D = 1.0$	$C/D = 0.5$
Centrifuge test	6.5–9.5	4.5–6.0	3.0–6.0
After Leca and Dormieux [15]	6.8–52.5	6.8–41.3	6.8–30.0
After Kirsch [11]	6.7–12.0	6.0–11.3	5.3–13.5
After Vermeer et al. [35]	7.5–10.5	7.5–10.5	7.5–10.5
After Anagnostou and Kovári [2]	6.0–12.7	6.0–12.4	3.0–12.0
After Chambon and Corté [5]	3.0–6.0	3.0–6.0	3.0–6.0

Table 3 Summary on ground deformation

DIC analysis	$C/D = 1.5$	$C/D = 1.0$	$C/D = 0.5$
Test No. for DIC analysis	T1	T5	T6
Standard error <0.5 [pixel]	0.449	0.035	0.040
Failure propagation after 5 mm piston displacement until	85 mm below surface	50 mm below surface	Surface
Inclination of wedge to horizontal δ [°]	68.0	66.5	64.0
Max. settlement [mm]	0.95	1.03	5.51

For an overburden ratio of $C/D = 1.0$ and $C/D = 1.5$, slip surfaces propagated until 50 mm and 100 mm below the surface, respectively. After a piston displacement of 3% of D, no noteworthy evolution of slip surfaces occurred (Fig. 12a). Instead of a further propagation of the shear zones, a funnel without sharply defined borders formed at ground surface.

The grain size might had some effect on the test result. The ratio of grain diameter, or alternatively the width of the shear band, to the width of the chimney is different to the ratio in the prototype. This may have some bearing when the support pressure is compared with the prototype. However, grain size has less effect on the failure mechanism.

Terzaghi [31, 32] explained the arching theory with a trap door model. The active mode was used to study the silo problem, which is similar to the earth pressure on a tunnel lining at a certain depth. For the three investigated overburden-to-diameter ratios, $C/D = 1.0$ seemed to mark a critical depth, since surface settlement was smaller than expected and similar to the settlement at a higher overburden pressure (Fig. 13). Therefore, some arching effects might have evolved. A similar threshold with the overburden equal to the tunnel diameter is also found in the literature (e.g., [12]).

5 Conclusions

The required face support for shallow tunnel in cohesionless soil was found to be dependent on the overburden, especially at a small piston displacement (<3% of D). Measured pressure at tunnel face was close to the upper bound solution for frictional material proposed by Léca and Dormieux [15], as well as to other experimental and analytical examinations. Since the minimum support pressure required for face stability was sought after, this finding is quite reasonable. However, one should be aware that the pressure measured in our experiment might underestimate the required support pressure due to reasons explained earlier.

Face collapse occurred in a narrow vertical band. The slip surface arising from tunnel invert propagated at an angle of about $45° + \varphi/2$ to the horizontal until it turned more or less vertical. The particle flow within the failure zone was oriented parallel to this slip surface.

Arching effects were observed to occur at an overburden ratio of $C/D = 1.0$. For smaller ratios, the unreduced body stress acted at tunnel face. At the overburden ratio $C/D = 1.0$ and $C/D = 1.5$, slip surfaces developed only marginally toward ground surface after a piston displacement of 3% of D. Further soil ingress was provided by a funnel formed at the ground surface. This resulted in the wider settlement trough observed at bigger overburden.

Acknowledgments This research was supported by the Austrian Geomechanics Society (ÖGG). The second author is grateful for the support from the Otto Pregl Foundation for Geotechnical Fundamental Research. The authors are grateful for the support from Malcolm Bolton and Stuart Haigh from Schofield Centre at Cambridge University.

References

1. Anagnostou G, Kovári K (1994) The face stability of slurry shield-driven tunnels. Tunn Undergr Space Technol 9(2): 165–174
2. Anagnostou G, Kovári K (1996) Face stability conditions with earth-pressure-balanced shields. Tunn Undergr Space Technol 11(2):165–173
3. Atkinson JH, Mair RJ (1981) Soil mechanics aspects of soft ground tunneling. Ground Eng 14(5):20–38
4. Bucky BP (1931) The use of models for the study of mining problems, Technical publication No.425, American institute of mining and metallurgical engineers, pp 3–28
5. Chambon P, Corté JF (1994) Shallow tunnels in cohesionless soil: stability of tunnel face. ASCE J Geotech Eng 120(7):1148–1165
6. Chambon P, Corté JF, Garnier J, König D (1991) Face stability of shallow tunnels in granular soils, Proceedings of the Centrifuge'91 Conference, 13–14 June. Boulder, Colorado, pp 99–105
7. Chambon P, Couillaud A, Munch P, Schürmann A, König D (1995) Stabilite′ du front de taille d'un tunnel: Étude de l'effet d'e′chelle, in Geo 95
8. Davis EH, Gunn MJ, Mair RJ, Seneviratne HN (1980) The stability of shallow tunnels and underground openings in cohesive material. Géotechnique 30(4):397–416
9. Horn M (1961) Horizontaler Erddruck auf senkrechte Abschlussflächen von Tunneln, in Landeskonferenz der ungarischen Tiefbauindustrie. German translation by STUVA, Düsseldorf
10. Kirsch A (2009) On the face stability of shallow tunnels in sand, Advances in geotechnical engineering and tunnelling No.16, Logos, Berlin
11. Kirsch A (2010) Experimental investigation of the face stability of shallow tunnels in sand. Acta Geotech 5(1):43–62
12. Kolymbas D (2005) Tunnelling and tunnel mechanics—a rational approach to tunnelling, Springer Verlag, Berlin
13. Kutter BL, Chang J-D, Davis BC (1995) Collapse of Cavities in Sand and Particle Size Effects, In: Proceedings international conference, Centrifuge '94, Singapore, Leung CF, Lee F-H, Tan TS (eds), Balkema, Rotterdam, pp 809–815
14. Krause T (1987) Schildvortrieb mit flüssigkeits- und erdgestützter Ortsbrust, No. 24 in Mitteilung des Instituts für Grundbau und Bodenmechanik der Technischen Universität Braunschweig
15. Leca E, Dormieux L (1990) Upper and lower bound solutions for the face stability of shallow circular tunnels in frictional material. Géotechnique 40(4):581–606
16. Lee KM, Rowe RK (1989) Deformations caused by surface loading and tunneling: the role of elastic anisotropy. Geotechnique 39(1):125–140
17. Ling HI (2010) A tribute to Philip Barnett Bucky (1899–1957) Father of centrifuge modeling in geomechanics. Acta Geotech 5(1):83–85
18. Mähr M (2006) Ground movements induced by shield tunneling in non-cohesive soils, Advances in geotechnical engineering and tunneling No. 15, Logos, Berlin
19. Mair RJ (1979) Centrifugal modelling of tunneling construction in soft clay, PhD Thesis, University of Cambridge
20. Mair RJ, Taylor RN (1997) Bored tunnelling in the urban environment. In: Proceedings of the 14th international conference on soil mechanics and foundation engineering, Hamburg, vol 4, pp 2353–2385
21. Mashimo H, Suzuki M (1998) Stability conditions of tunnel face in sandy ground. In: Proceedings of the centrifuge '98 conference, Tokyo, Japan, 23–25 September, pp 721–725
22. Meguid MA, Saada O, Nunes MA, Mattar J (2008) Physical modeling of tunnels in soft ground: a review. Tunn Undergr Space Technol 23(2):185–198
23. Mélix P (1987) Modellversuche und Berechnungen zur Standsicherheit oberflächennaher Tunnel, Veröffentlichungen des Institutes für Bodenmechanik und Felsmechanik der Universität Fridericiana, Karlsruhe
24. Park SH, Adachi T, Kimura M, Kishida K (1999) Trap door test using aluminum blocks. In: Proceedings of the 29th symposium of rock mechanics J.S.C.E., pp 106–111
25. Plekkenpol JW, van der Schrier JS, Hergarden HJ (2006) Shield tunnelling in saturated sand - face support pressure and soil deformations. In: Bezuijen A, van Lottum H (eds) Tunnelling: a decade of progress, GeoDelft 1995–2005. Taylor & Francis, London
26. Rowe RK, Kack GJ (1983) A theoretical examination of the settlements induced by tunneling: from cases history. Can Geotech J 20(2):299–314
27. Sterpi D, Cividini A, Sakurai S, Nishitake S (1996) Laboratory model tests and numerical analysis of shallow tunnels, In: Proceedings of the international symposium on eurock '96—ISRM, Torino, Vol.1. Balkema, Rotterdam, pp 689–696
28. Stone KJL, Muir Wood D (1992) Effects at dilatancy and particle size observed in model tests on sand. Soils Found 32(4):43–47

29. Taylor RN (1995) Geotechnical centrifuge technology. Blackie academic and professional, Glasgow
30. Technical Commitee 2 of ISSMGE—Physical modelling in geotechnics (2007) Catalogue of scaling laws and similitude questions in centrifuge modelling
31. Terzaghi K (1936) Stress distribution in dry and in saturated sand above a yielding trap-door. In: Proceedings of the international conference on soil mechanics, Vol. 1. Harvard University. Press, Cambridge, MA, pp 307–311
32. Terzaghi K (1943) Theoretical Soil Mechanics. Wiley, New York
33. Thusyanthan I, White DJ, Take WA (2008) Deformation measurement using digital imaging and PIV (Particle Image Velocimetry) technique, Lecture sheets, University of Cambridge
34. Vardoulakis I, Graf B, Gudehus G (1981) Trap-door problem with dry sand: a statical approach based upon model test kinematics. Int J Numer Anal Methods Geomech 5:57–78
35. Vermeer P, Ruse N, Marcher T (2002) Tunnel heading stability in drained ground. Felsbau 20(6):8–24
36. White DJ, Take WA (2002) GeoPIV: Particle Image Velocimetry (PIV) Software for use in geotechnical testing, Technical report, University of Cambridge
37. White DJ, Take WA, Bolton MD (2001) Measuring soil deformation in geotechnical models digital images and PIV analysis, 10th International Conference on Computer Methods and Advances in Geomechanics. Tuscan, Arizona, pp 997–1002
38. White DJ, Take WA, Bolton MD (2003) Soil deformation measurement using particle image velocimetry (PIV) and photogrammetry. Géotechnique 53(7):619–631
39. White RJ, Stone KJL, Jewell JJ (1994) Effect of particle size on localisation development in model tests on sand, In: Proceedings international conference, centrifuge '94, Singapore, Leung CF, Lee F-H, Tan TS (eds), Balkema, Rotterdam, pp 817-822